

Article

Cu-Metalated Porphyrin-Based MOFs Coupled with Anatase as Photocatalysts for CO₂ Reduction: The Effect of Metalation Proportion

Maria Anagnostopoulou ¹, Valérie Keller ¹  and Konstantinos C. Christoforidis ^{1,2,3,*} 

¹ Institut de Chimie et Procédés Pour l’Energie, l’Environnement et la Santé, (ICPEES) UMR7515 CNRS, ECPM, University of Strasbourg, 25 Rue Becquerel, Cedex 2, 67084 Strasbourg, France; managnostopoulou@unistra.fr (M.A.); vkeller@unistra.fr (V.K.)

² Department of Environmental Engineering, Democritus University of Thrace, Vas. Sofias 12, 67132 Xanthi, Greece

³ Chemical Process & Energy Resources Institute, Centre for Research & Technology Hellas, 57001 Thessaloniki, Greece

* Correspondence: kochristo@env.duth.gr

Abstract: Converting carbon dioxide (CO₂) into valuable chemicals such as fossil resources via photocatalysis requires the development of advanced materials. Herein, we coupled zirconium-based metal–organic frameworks (MOFs) containing porphyrin and Cu-porphyrin with anatase TiO₂. The effect of the porphyrin metalation proportion was also investigated. Notably, while the use of free-base porphyrin as the organic linker resulted in the development of PCN-224, the presence of Cu-porphyrin provided mixed-phase MOF structures containing both PCN-224 and PCN-222. MOF/TiO₂ composites bearing partial (50%) metalated porphyrin were proven more active and selective towards the production of CH₄, at ambient conditions, in the gas phase and using water vapors without the use of hole scavengers. The optimized composite bearing 15 wt.% of the partial metalated MOF was three times more active than pure TiO₂ towards CH₄ production. This study provides insights on the effect of precise materials engineering at a molecular level on the development of advanced MOF-based photocatalysts for CO₂ reduction.

Keywords: metal–organic frameworks; CO₂; composites; TiO₂; photocatalysis; PCN; metalated porphyrin



Citation: Anagnostopoulou, M.; Keller, V.; Christoforidis, K.C.

Cu-Metalated Porphyrin-Based MOFs Coupled with Anatase as

Photocatalysts for CO₂ Reduction: The Effect of Metalation Proportion.

Energies **2024**, *17*, 1483. <https://doi.org/10.3390/en17061483>

Received: 29 January 2024

Revised: 17 February 2024

Accepted: 13 March 2024

Published: 20 March 2024



Copyright: © 2024 by the authors. Licensee MDPI, Basel, Switzerland. This article is an open access article distributed under the terms and conditions of the Creative Commons Attribution (CC BY) license (<https://creativecommons.org/licenses/by/4.0/>).

1. Introduction

Currently, there is a great need for alternatives to deal with the increasing global energy requirements, the fossil resource depletion, but mostly the environmental crisis originating from the rapid CO₂ accumulation in the atmosphere due to fossil fuel usage. To this end, photocatalysis has the potential to contribute both to clean energy production and to the utilization of CO₂ as a cheap and easily available carbon-source, converting it into valuable feedstocks [1]. This process greatly depends on the properties of the photocatalysts used. Therefore, many different types of materials have been developed and applied in CO₂ photocatalytic reduction. As in other photocatalytic reactions, TiO₂ has been intensively studied in CO₂ reduction [2–4]. However, inherent drawbacks related to fast charge carriers’ recombination and UV-light response prevent further application of TiO₂. Different strategies have been applied to develop improved TiO₂-based photocatalysts for CO₂ reduction including modification via ion doping [5], surface engineering [6], photosensitization [7] and formation of composites and heterojunctions [3,8]. The latter approach synergizes materials, offering the possibility to develop advanced systems and improve the properties of traditional catalysts such as TiO₂ [9].

Over the last decade, the interest in metal–organic frameworks (MOFs) as heterogeneous photocatalysts has grown significantly, mostly due to their tunable properties and high specific surface area that facilitates adsorption [10–12]. MOFs have been applied as

photocatalysts either individually [10,12–14] or as part of a composite material [9–11,15] for CO₂ reduction. TiO₂-based hybrid photocatalysts bearing MOF structures have been developed and tested in CO₂ reduction as a way to integrate increased light harvesting, active catalytic sites and high surface areas [3,9,16–18], presenting superior activity in CO₂ reduction but also in selectivity towards C-products. Improvements in several important parameters have been reported that enhanced CO₂ conversion in such composite materials [9,16,18]. Among the different MOFs studied, of particular importance are stable structures that contain porphyrins as organic linkers. These structures offer the advantage of visible light absorption capacity [19,20], the ability for efficient and fast exciton migration and transportation from the photoexcited porphyrin moiety to suitable catalysts [21,22] and the presence of a metalation center [23] that may affect the electronic properties and control catalytic activity.

Porphyrinic zirconium MOFs have been studied in CO₂ photocatalytic reduction [14,23–25]. The Zr ions in the metal clusters may have multiple redox states (i.e., 4+ or 3+) [23,25] and act as semiconductors while the photoexcited porphyrin linker can activate these clusters [25–27]. Heterojunctions have been developed via the coupling of such MOF structures with other photocatalysts [18,27], improving charge recombination phenomena. In addition, metalation of the porphyrin linker as well as the degree of metalation (partial metalated porphyrins) may also affect the overall photocatalytic activity [19,23,28–30].

In view of the recent contributions and driven by the different possibilities to tune the activity of porphyrin MOF/TiO₂ photoactive materials, a series of porphyrinic-MOF/TiO₂ composite materials were prepared by adjusting the degree of metalation using free-base or copper-metalated porphyrin as the linker. It is shown that both photocatalytic activity and selectivity towards H₂, CO and CH₄ may be controlled by varying the metalation degree of the porphyrin linker.

2. Materials and Methods

Zirconium chloride, benzoic acid and N,N-Dimethylformamide (anhydrous, 99.8%), Cu(NO₃)₂•3H₂O and tetra(4-carboxylphenyl)porphyrin (H₂TCPP) were supplied by Sigma Aldrich, Burlington, MA, USA. TiO₂ (Hombikat UV100) was purchased from Sachtleben Chemie GmbH (Duisburg, Germany). The chemical reagents were used without further purification.

2.1. H₂TCPP Metalation

Metalation of the H₂TCPP was performed using a reported protocol with small modifications [31]. Specifically, 0.3047 g of Cu(NO₃)₂•3H₂O and 0.1970 g H₂TCPP were dissolved in 15 mL of DMF. The mixture was heated at 150 °C under reflux for 5 h. Then, the solution was cooled down naturally, and the precipitate was collected by filtration and was rinsed with DMF and EtOH. The complex formed was labeled CuTCPP.

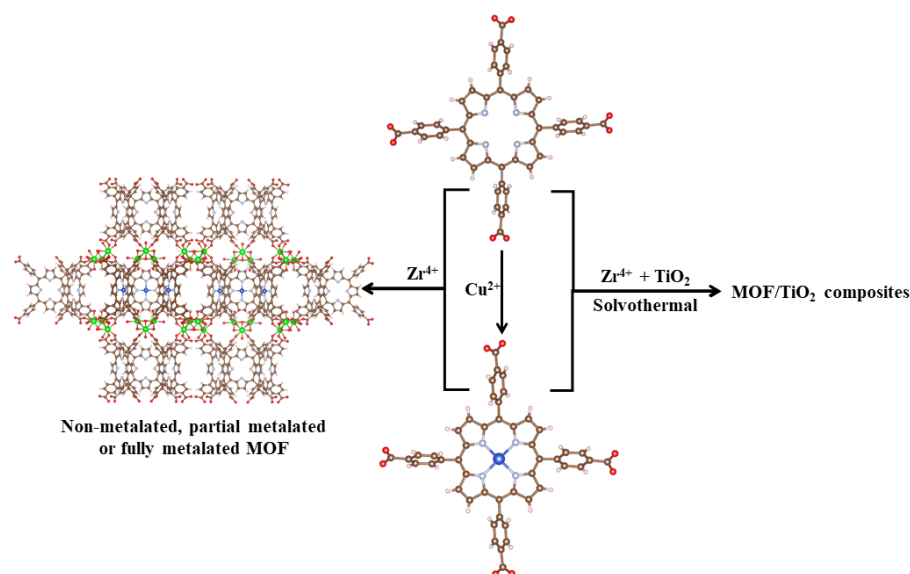
2.2. MOF Synthesis

MOF structures were synthesized using a typical protocol already reported in the literature for the development of PCN-224 [32]. Specifically, a mixture of 0.173 g H₂TCPP, 0.288 g ZrCl₄ and 9.73 g benzoic acid was dissolved in 29 mL DMF and put in sonication till all the precursors were dissolved. Then, the solution was transferred to a 90 mL teflon-lined stainless steel autoclave and heated at 120 °C for 48 h. After cooling down, the resultant black powder was collected with filtration and washed several times with fresh DMF and, finally, with acetone. Then, the powder was vacuum dried at 120 °C overnight to remove any remaining solvent. For the development of the MOF structure containing the metalated porphyrin, the same procedure was followed, but CuTCPP was used. Two different approaches were used, where the organic ligand concentration was identical to the synthesis using the free-base H₂TCPP. In the first, a molar ratio of H₂TCPP:CuTCPP equal to 1:1 was used, while in the second, only CuTCPP was used.

The resulted MOFs were denoted as MOF-a, MOF-b and MOF-c using only H₂TCPP, H₂TCPP:CuTCPP at 1:1 molar ratio and only CuTCPP, respectively.

2.3. Synthesis of MOF/TiO₂ Composite Materials

The development of the composites was performed by in situ synthesis of the MOF structure in the presence of TiO₂, using the same protocol as the one used for the pure MOF synthesis. The precursors of the MOF structure were mixed with 1.663 g of TiO₂ powder and sonicated for 30 min. Three composite materials were developed by adding either H₂TCPP, a mixture of H₂TCPP:CuTCPP at 1:1 molar ratio or only CuTCPP. The composites were denoted as MOF-a/TiO₂, MOF-b/TiO₂ and MOF-c/TiO₂ using H₂TCPP, a mixture of H₂TCPP:CuTCPP or only CuTCPP as precursors, respectively. An illustration depicting the steps used in the synthesis protocol is given in Scheme 1.



Scheme 1. Schematic illustration of the synthesis protocol used to develop the MOFs and composite materials.

2.4. Pt Deposition

The introduction of Pt (1 wt.%) was realized by a chemical reduction deposition method, using H₂PtCl₆ and NaBH₄ as the reducing agent following a process already reported [4].

2.5. Materials Characterization

X-ray diffraction (XRD) patterns were recorded using a Bruker D8-Advance (Karlsruhe, Germany) diffractometer equipped with a scintillation counter detector, with a Cu-K α radiation. Attenuated Total Reflectance IR spectra were measured with a Thermo Fisher Nicolet iS10 spectrometer (Waltham, MA, USA). Nitrogen adsorption–desorption isotherms were obtained using a Micromeritics Asap 2420 porosimeter (Norcross, GA, USA) at 77 K. Prior to the analysis, the samples were degassed at 150 °C under vacuum for 5 h. Thermogravimetric analyses (TGA) were performed using a TA Instrument Q5000IR (New Castle, DE, USA) under the air flow (flow rate of 25 mL·min^{−1}) with the temperature ranging from 50 to 600 °C, with a dynamic ramping rate depending on the weight loss. Diffuse Reflectance UV-vis absorption spectra were recorded in the range of 200–800 nm using a PerkinElmer Lambda 950 Scan spectrophotometer (Waltham, MA, USA) equipped with integrating sphere using BaSO₄ as a reference; the energy bandgap was calculated by using the Tauc plot. A Zeiss Gemini SEM 500 (Munich, Germany) equipped with FEG Schottky was used for Scanning Electron Microscopy. X-ray photoelectron spectroscopy (XPS) measurements were performed on an ultrahigh vacuum (UHV) Thermo-VG scientific

Spectrometer source, and the spectra were calibrated by the Adventitious Carbon peak at 284.6 eV. A Zeiss Gemini SEM 500 equipped with FEG Schottky was used for Scanning Electron Microscopy.

2.6. Photocatalytic Reactions

The photocatalytic evaluation was performed under continuous flow conditions. Fifty mg of the catalyst suspension was drop-casted on a glass disc and dried under vacuum for 2 h at 100 °C. The disc was then placed in a stainless-steel reactor (6 mL) that was irradiated from the top through a quartz glass window. A defined flow (0.3 mL·min⁻¹) of research-grade CO₂ was passed through a thermo-controlled water saturator, feeding the reactor. Prior to the test, the reactor was purged with CO₂/H₂O till all impurities were eliminated. During the test, a Hg lamp (150 W, Ceramic-Metal-Halide, C-Topspot, StrassElec SARL, Strasbourg, France) simulating solar light was used as an irradiation source (irradiances in the 300–800 nm region: UV = 46 W·m⁻², Visible = 4271 W·m⁻², the emission spectrum is given in Figure S1). The evolved gases were analyzed every 15 min by a micro-GC (Agilent 3000 A SRA Instrument, Santa Clara, CA, USA).

3. Results and Discussion

Figure S2a presents the UV-Vis spectra of the H₂TCPP before (free-base) and after the metalation (CuTCPP). The H₂TCPP presented an intense Soret band centered at ca. 415 nm and four Q bands (516, 555, 580 and 635 nm), typical of the free-base H₂TCPP. After metalation, a blue shift of the Soret band and the presence of only two Q-bands were evidenced for the CuTCPP complex. This observation suggests the successful incorporation of copper in the porphyrin core [33]. To further evidence the TCPP metalation, infrared spectra were also recorded (Figure S2b). The peak centered at 966 cm⁻¹ assigned to the N–H in-plane bending vibration of pyrrolic nitrogen became undetectable after the treatment with Cu²⁺, suggesting an interaction between the –NH groups inside the porphyrin ring and copper ions [34–36]. In addition, a peak at ca. 1000 cm⁻¹ was detected at the CuTCPP complex that is assigned to the bond stretching/bending vibration between Cu²⁺ and TCPP ligand [37]. The shift of the peak at 1685 cm⁻¹ to 1654 cm⁻¹ and the presence of a strong peak at 1400 cm⁻¹ suggest alteration of the –COOH groups of the porphyrin ring, probably via the interaction with Cu²⁺ ions. As will be shown later, this did not affect the development of the MOF structure. Therefore, both UV-Vis and ATR spectroscopies verified the successful coordination of Cu²⁺ within the porphyrin core.

XRD analysis was then performed in order to get information on the structure of both TiO₂ and the MOF synthesized. The diffraction patterns are given in Figure 1. A typical diffraction pattern of PCN-224 was acquired for the material synthesized using only the free-base H₂TCPP, i.e., MOF-a [38]. In the MOF-b and MOF-c, an increase in the diffraction peak width was evidenced with increasing the CuTCPP content. In addition to this, the intensity of the peak centered at ca. 7.2° increased going from MOF-b to MOF-c, and a peak centered at ca. 9.9° was clearly observed. These new peaks are fingerprints of the PCN-222 structure [39] and suggest the presence of more than one porphyrinic MOFs when CuTCPP is used. More particular, in addition to the PCN-224, PCN-222 was also formed using the CuTCPP complex in the synthesis process [39,40]. As expected, the TiO₂ was of pure anatase phase. Close inspection of the anatase (101) main diffraction peak centered at ca. 25.4° revealed that the synthesis employed for the development of the MOF did not alter the characteristics of the TiO₂ phase in terms of phase composition and crystallinity. This is probably related to the mild conditions applied for the development of the MOF. The XRD patterns of all nanocomposite materials contained the diffraction peaks of the two individual counterparts, as displayed in Figure 1b. The low intensity of the diffraction peaks corresponding to the MOF structure probably originates from the low MOF amount in the final composite material.

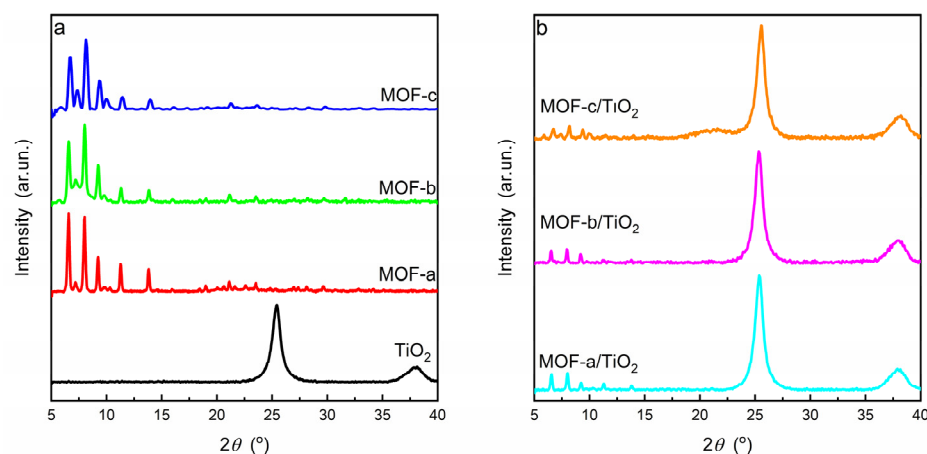


Figure 1. XRD patterns of (a) pure TiO₂ and MOFs and (b) nanocomposite materials.

Further evidence for the presence of both phases in the composites was obtained from ATR spectroscopy (Figure S3). Typical spectra of the pure TiO₂ and porphyrin MOFs were acquired. Interestingly, the peak centered at ca. 1683 cm⁻¹ that corresponds to the C=O stretching vibration from the carboxyl functional groups greatly weakened in the MOF spectra when compared with the H₂TCPP, suggesting the successful coordination of the porphyrin's -COOH groups with Zr to form the MOF crystal [41,42]. Most importantly, the peak centered at ca. 1000 cm⁻¹, assigned to the successful coordination of Cu²⁺ in the porphyrin core was also detected in the MOFs prepared by using in part or only CuTCPP as the organic linker [43]. This was accompanied by the disappearance of the peak assigned to the N-H in-plane bending vibration of pyrrolic nitrogen (centered at ca. 963 cm⁻¹) [34–36] that was only observed in the MOF-a material developed using the free-base H₂TCPP. These data suggest that Cu²⁺ remained in the porphyrin core even after the development of the MOF structure. TiO₂ gave rise to a featureless broad peak at low wavenumbers (400–920 cm⁻¹) that was also evidenced in the composite materials [44]. As in the case of XRD, the ATR spectra of the composite materials contained features from the two individual counterparts.

Light absorption properties were studied by means of UV–vis diffuse reflectance spectroscopy (DRS). The corresponding spectra are given in Figure S4. The light absorption onset of the pure TiO₂ was below 400 nm corresponding to a band gap energy (E_g) of ca. 3.20 eV, typical for pure anatase materials. On the contrary, light absorption extended to the whole visible region for the pure MOF materials. This is due to the Soret and the Q bands of the porphyrin linker that absorb light from 350 up to 800 nm [45]. Similar light absorption properties were also evidenced for all composites. These findings clearly suggest that the extension of light absorption to the visible region detected for the composite materials can be solely attributed to the presence of the MOF structure.

Furthermore, differences were also detected in the absorption in the visible light region when comparing the MOF structures developed using the free-base H₂TCPP and the CuTCPP complex. Specifically, the four Q bands detected on the MOF structure where the free-base TCPP ligand was used were converted into two, both in the pure MOFs and the composite materials. This is in line with results in the literature where metalated porphyrins were used to develop porphyrinic MOF structures [43,45]. These findings further suggest that the porphyrin core was metalated in the MOFs where CuTCPP was used as the organic linker, in agreement with the ATR results.

Quantification of the two parts in the final composites was performed by thermogravimetric analysis (TGA). Representative TGA profiles are given in Figure S5. The small mass drop up to 200 °C can be attributed to impurities on the surface of TiO₂ and guest species in the MOF structures. The temperature onset of the organic decomposition in the pure MOFs is observed at ca. 425 °C. This is slightly shifted to lower values in the composites, probably due to the presence of the oxide. The remaining weight at 600 °C was used to

calculate the content of the MOF in the hybrid materials. This was practically constant within the three composite samples ranging from (13 to 15 wt.%).

The composition of the prepared materials was further investigated using XPS. The survey spectra revealed the presence of Ti, O, C, N, Zr and Cu in the corresponding samples (Figure S6). Cu was only detected in the MOF structures where CuTCPP was used as the organic ligand. High resolution XPS spectra are shown in Figure 2. The peak centered at 184.7 and 182.3 eV are ascribed to Zr 3d_{3/2} and Zr 3d_{5/2}. The Zr peaks were shifted to lower binding energies in the case of the composite materials compared to the signal recorded for the bare MOFs. Similarly, the Ti 2p peak in the composite materials was shifted to higher binding energies (ca. 0.2 eV), compared to the Ti 2p_{3/2} of the pure TiO₂ (Figure 2b). This observation indicates a strong interaction between the MOF and TiO₂ and suggests the presence of a pathway for charge transfer between the two parts of the composite [46]. High resolution XPS spectra in the 402–397 eV region revealed the presence of N-species from the organic linker (Figure 2c). Two peaks were observed for MOF-a. More precisely, the peak at ca. 397.8 eV originates from the iminic nitrogen (–C=N–), and the peak at 400 eV is ascribed to pyridinic nitrogen (–NH–) of the free-base porphyrin [47]. The N 1s spectrum of the MOF-c, developed using the metalated CuTCPP as the organic linker, presented only one peak, attributed to N interacting with Cu [48], centered between the two peaks of free-base porphyrin at 398.4 eV [49]. This further verifies that the porphyrin remained metalated even after the synthesis of the MOF, in agreement with ATR and DRS-UV-Vis. Finally, based on XPS surface composition analysis, the Cu content was estimated to be 0.47% in the pure MOF-c and 0.06% in the corresponding MOF-c/TiO₂ composite. This is expected, taking into account the ca. 15% of the MOF-c in the MOF-c/TiO₂ composite, as extracted from TGA.

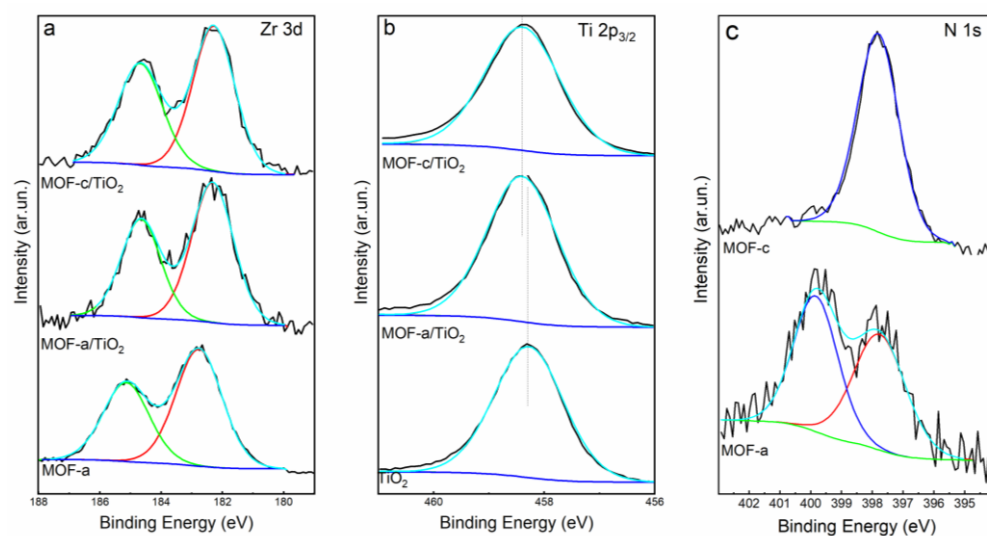


Figure 2. High resolution XPS spectra of Zr 3d (a), Ti 2p_{3/2} (b) and N 1s (c) of the prepared pure and composite materials and the corresponding simulated spectra.

N₂ sorption–desorption isotherms were contacted to evaluate the textural properties (Figure S7). The MOF-a material developed using only H₂TCPP as the organic linker presented a type I isotherm indicating microporosity [35] and a Brunauer–Emmett–Teller (BET) surface area of 1617 m² g^{−1}. On the contrary, MOF-c presented a type IV isotherm, with two plateaus at ca. P/P₀ = 0.3 and a slightly increased BET surface area (1739 m² g^{−1}). The presence of mesoporosity is characteristic of the PCN-222 structure [39] and is in line with the XRD results. Surface area significantly decreased in all composite materials, with the isotherm resembling that of the pure TiO₂, probably due to the low MOF content.

To further establish the formation of composites and to elucidate morphological characteristics that may have given rise to the different textural properties and crystal structures, a microscopy analysis of the prepared materials was undertaken. Figure 3 presents SEM images of the pure MOF structures. A cubic morphology in the range of micrometers was evidenced for the MOF-a material developed using H₂TCPP, typical of the PCN-224 structure (Figure 3a). In addition to the cubes that were clearly formed when CuTCPP was used in the synthesis process, needle-shaped crystals were also observed (MOF-b and MOF-c, Figure 3b–d). Their length varied from a few up to tenths of micrometers and their width from hundreds of nanometers up to a few micrometers. Particles of this morphology are ascribed to the formation of PCN-222 [39], revealing that MOF-b and MOF-c are mixed phase materials containing both PCN-224 and PCN-222. These two MOFs have identical building units but differ in topology [14]. The PCN-222 content as well as the size of the needle-shaped particles increased by increasing the CuTCPP content during the synthesis. In addition, more uniform-sized PCN-222 particles and less resolved cubic particles were detected in the MOF-c material when compared with the MOF-b. This clearly suggests that the use of CuTCPP as the organic linker precursor favors the formation of PCN-222 under the conditions of our experiment. Formation of PCN-222 also explains the two plateaus in the N₂ isotherms and the mesoporosity observed for the MOF-b and MOF-c materials.

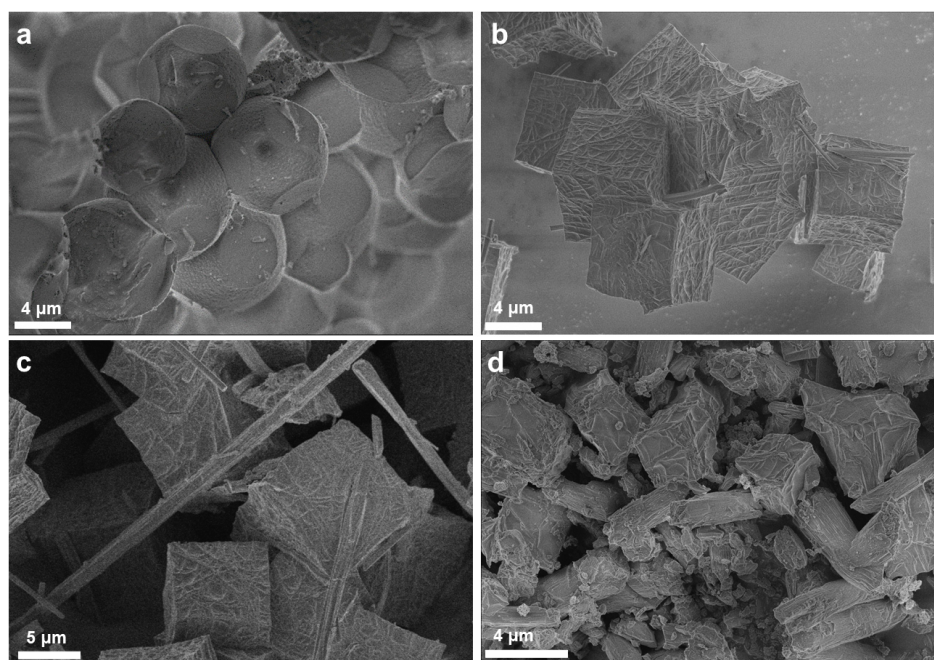


Figure 3. SEM images of the MOF-a (a), MOF-b (b,c) and the MOF-c (d) materials.

These morphological characteristics were maintained in the composite materials (Figure 4). In addition to the MOF particles, large TiO₂ agglomerates of few micrometers were observed in all three composites. Well dispersed TiO₂ particles on the surface of the MOFs were also resolved, forming agglomerates of significantly smaller size. For example, the size of TiO₂ agglomerates in the pure TiO₂ ranged between few hundreds of nanometers to micrometers, while agglomerates in the nanometer scale were detected on the surface of the MOF particles in the composites (Figure 4f). This may affect catalytic activity due to the increase in the exposed active sites due to the smaller TiO₂ agglomerates in the composites [50].

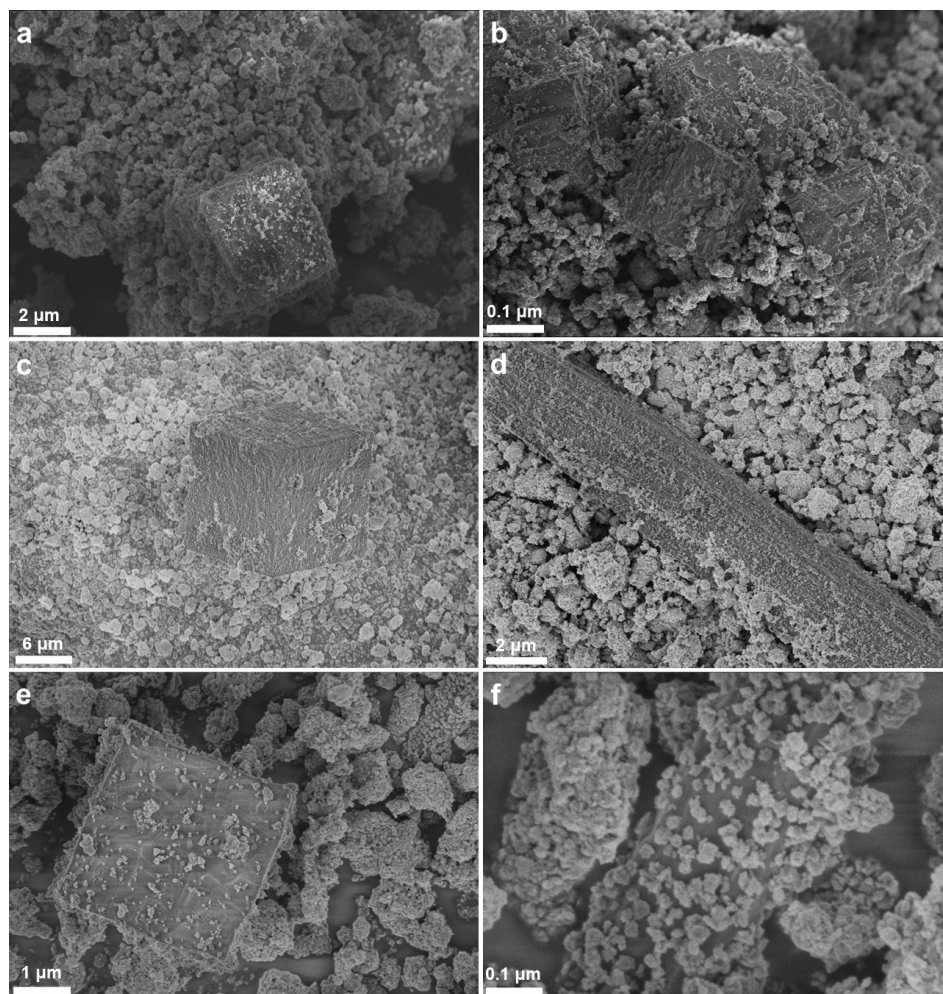


Figure 4. SEM images of the MOF-a/TiO₂ (a,b), MOF-b/TiO₂ (c,d) and the MOF-c/TiO₂ (e,f) composite materials.

Following the characterization, all materials were tested as photocatalysts for the reduction of CO₂ in gas phase using water vapor as the electron donor. Under these conditions, H₂, CO and CH₄ were only detected in the gas phase. Figure 5 presents the average production rates of the catalytic reactions performed over 10 h using the pure TiO₂ and the three composite materials. Under the same catalytic conditions, no products were detected using the pure MOF structures. Only H₂ and minimal amount of CH₄ were detected using the MOF-a/TiO₂ and the pure TiO₂. Photocatalytic activity improved significantly when CuTCPP was used in the synthesis process. Specifically, H₂ and CH₄ production increased five and three times in the MOF-b/TiO₂ compared with the TiO₂ and MOF-a/TiO₂ composite. In addition, CO was also detected in the gas phase. Photocatalytic activity for H₂ and CH₄ production decreased in the MOF-c/TiO₂ compared with the MOF-b/TiO₂; however, it was higher compared with the pure TiO₂ and the MOF-a/TiO₂ composite. The smaller PCN-222 crystals observed in MOF-b compared with MOF-c (Figure 3) could play a role in the improved catalytic activity. Besides activity, the selectivity among the C-products was also improved towards CH₄ production using the MOF-b/TiO₂ compared with the MOF-c/TiO₂. The increased catalytic activity of the MOF-b/TiO₂ and MOF-c/TiO₂ is also evidenced in Figure S8, which presents the total e⁻ utilized by the catalysts taking into account all reaction products (H₂, CH₄ and CO). The use of the metalated CuTCPP complex resulted in an impressive enhancement in activity. The MOF-b/TiO₂ composite presented the highest activity, an approximately 4-fold increase compared to the reference pure TiO₂ catalyst. These results are in accordance with recent

contributions to the literature. PCN-222 has been previously reported more active in CO₂ photocatalytic reduction compared with PCN-224 using a light sensitizer [14]. In addition, partial metalated porphyrins have been also proven more active in photocatalytic CO₂ reduction using a hydrogen-bonded organic framework [29].

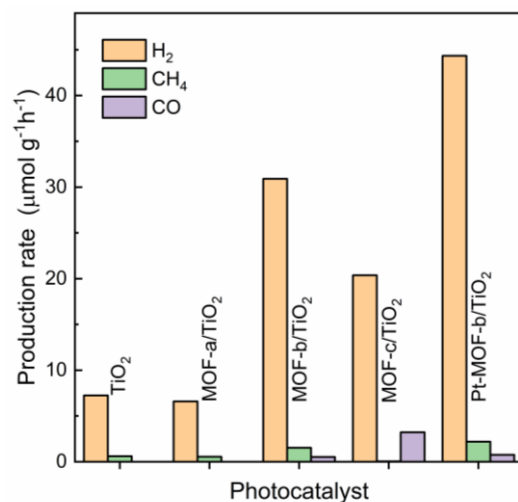


Figure 5. Photocatalytic activity of the prepared materials.

Of importance is to mention that no carbon-products were detected when CO₂ was replaced with argon. This clearly evidences that the C-products detected in the gas phase using the composite materials as catalysts originate from CO₂ and not from any carbons on the surface of TiO₂ or the MOF structure. Furthermore, to exclude the effect of the porphyrin ligand acting simply as an antenna, a TiO₂ material loaded with porphyrin was prepared and tested, resulting in no production of any gaseous products. This reference reaction provides clear evidence for the beneficial effect of the MOF in the observed increased activity of the composite materials. Finally, since Pt nanoparticles have been widely applied as co-catalyst in similar reactions, the best performing composite was loaded with 1 wt.% Pt. It is generally accepted that Pt improves charge separation efficiency acting as an e⁻ sink. The presence of Pt increased H₂ and CH₄ production by ca. 50%, which could be assigned to the improved charge availability.

Several parameters could contribute to improved catalytic efficiency. The integrated MOF structure in the composite provided extension of the light harvesting to the visible region [18]. Formation of a heterojunction in such a type of composites may improve charge handling properties [9,32,50,51]. The conduction band (CB) and valence band of both PCN-224 and PCN 222 have been reported to be less positive than that of anatase [18,23,32]. Therefore, taking into account that both TiO₂ and MOF are excited under artificial solar light irradiation and the tight interaction of the two parts in the composite as revealed by XPS, efficient charge separation may take place due to their matched band structure [18,23,32]. In addition, the presence of CuTCPP complex as an organic ligand in the MOF structure could also function as a catalytic site, improving CO₂ reduction and H₂ production [52]. Regarding the effect of the relative CuTCPP portion, it has been recently demonstrated in similar structures that the CuTCPP/H₂TCPP loading ratio affects greatly the charge carrier separation efficiency where charge is transferred from the free-base H₂TCPP to the CuTCPP [29]. This could also improve charge formation and separation MOFs containing both H₂TCPP and CuTCPP. All these parameters could contribute in the observed improved catalytic activity.

4. Conclusions

For the first time, porphyrinic zirconium MOF/TiO₂ composites controlling the free-base porphyrin/metalloporphyrin (CuTCPP) loading ratio were developed. Detailed

characterization of the prepared materials revealed that the use of CuTCPP as the organic linker resulted in the development of mixed phase MOFs, allowing the development of both PCN-224 and PCN-222. Photocatalytic activity evaluation revealed that the use of metalated porphyrin as well as regulating the proportion significantly affects CO₂ reduction efficiency and selectivity, presenting a 5- and 3-fold increased H₂ and CH₄ production, respectively, compared with the pure TiO₂ or composites with MOF structures bearing only the free-base porphyrin.

Supplementary Materials: The following supporting information can be downloaded at: <https://www.mdpi.com/article/10.3390/en17061483/s1>, Figure S1: Irradiance spectra; Figure S2: UV-Vis (a) and ATR (b) spectra of the of the H₂TCPP and CuTCPP complex; Figure S3: ATR spectra of TiO₂, pure MOFs and composite nanomaterials; Figure S4: DR-UV-Vis spectra of the pure MOFs and TiO₂ and composite materials; Figure S5: TGA profile of TiO₂, synthesized MOFs and composite materials; Figure S6: Survey spectra of the prepared materials; Figure S7: Nitrogen sorption/desorption isotherms; Figure S8: electrons used in the reactions.

Author Contributions: Conceptualization, K.C.C.; methodology, K.C.C.; software, V.K.; validation, M.A.; formal analysis, M.A., V.K. and K.C.C.; investigation, M.A.; resources, V.K. and K.C.C.; data curation, M.A.; writing—original draft preparation, M.A.; writing—review and editing, V.K. and K.C.C.; visualization, M.A. and K.C.C.; supervision, V.K. and K.C.C.; project administration, K.C.C.; funding acquisition, K.C.C. All authors have read and agreed to the published version of the manuscript.

Funding: This research benefited from state aid managed by the French National Research Agency (ANR) under the Investments for the Future (program “Make Our Planet Great Again”) with reference ANR-18-MOPGA-0014. This research has received funding from the European Union under grant agreement No. 101099717—ECOLEFINS project.

Data Availability Statement: The data presented in this study are available on request.

Conflicts of Interest: The authors declare no conflicts of interest.

References

1. Sayre, H.J.; Tian, L.; Son, M.; Hart, S.M.; Liu, X.; Arias-Rotondo, D.M.; Rand, B.P.; Schlau-Cohen, G.S.; Scholes, G.D. Solar Fuels and Feedstocks: The Quest for Renewable Black Gold. *Energy Environ. Sci.* **2021**, *14*, 1402–1419. [[CrossRef](#)]
2. Habisreutinger, S.N.; Schmidt-Mende, L.; Stolarczyk, J.K. Photocatalytic Reduction of CO₂ on TiO₂ and Other Semiconductors. *Angew. Chem. Int. Ed.* **2013**, *52*, 7372–7408. [[CrossRef](#)] [[PubMed](#)]
3. Duflot, M.; Marchal, C.; Caps, V.; Artero, V.; Christoforidis, K.; Keller, V. Optimization of NH₂-UiO-66/TiO₂/Au Composites for Enhanced Gas-Phase CO₂ Photocatalytic Reduction into CH₄. *Catal. Today* **2023**, *413–415*, 114018. [[CrossRef](#)]
4. Ioannidou, T.; Anagnostopoulou, M.; Vasiliadou, I.A.; Marchal, C.; Alexandridou, E.-O.; Keller, V.; Christoforidis, K.C. Mixed Phase Anatase Nanosheets/Brookite Nanorods TiO₂ Photocatalysts for Enhanced Gas Phase CO₂ Photoreduction and H₂ Production. *J. Environ. Chem. Eng.* **2024**, *12*, 111644. [[CrossRef](#)]
5. Xin, X.; Xu, T.; Wang, L.; Wang, C. Ti³⁺-Self Doped Brookite TiO₂ Single-Crystalline Nanosheets with High Solar Absorption and Excellent Photocatalytic CO₂ Reduction. *Sci. Rep.* **2016**, *6*, 23684. [[CrossRef](#)] [[PubMed](#)]
6. Low, J.; Cheng, B.; Yu, J. Surface Modification and Enhanced Photocatalytic CO₂ Reduction Performance of TiO₂: A Review. *Appl. Surf. Sci.* **2017**, *392*, 658–686. [[CrossRef](#)]
7. Ola, O.; Maroto-Valer, M.M. Review of Material Design and Reactor Engineering on TiO₂ Photocatalysis for CO₂ Reduction. *J. Photochem. Photobiol. C Photochem. Rev.* **2015**, *24*, 16–42. [[CrossRef](#)]
8. Wei, L.; Yu, C.; Zhang, Q.; Liu, H.; Wang, Y. TiO₂-Based Heterojunction Photocatalysts for Photocatalytic Reduction of CO₂ into Solar Fuels. *J. Mater. Chem. A Mater.* **2018**, *6*, 22411–22436. [[CrossRef](#)]
9. Crake, A.; Christoforidis, K.C.; Kafizas, A.; Zafeiratos, S.; Petit, C. CO₂ Capture and Photocatalytic Reduction Using Bifunctional TiO₂MOF Nanocomposites under UV-Vis Irradiation. *Appl. Catal. B* **2017**, *210*, 131–140. [[CrossRef](#)]
10. Swetha, S.; Janani, B.; Khan, S.S. A Critical Review on the Development of Metal-Organic Frameworks for Boosting Photocatalysis in the Fields of Energy and Environment. *J. Clean. Prod.* **2022**, *333*, 130164. [[CrossRef](#)]
11. Qian, Y.; Zhang, F.; Pang, H. A Review of MOFs and Their Composites-Based Photocatalysts: Synthesis and Applications. *Adv. Funct. Mater.* **2021**, *31*, 2104231. [[CrossRef](#)]
12. Navalón, S.; Dhakshinamoorthy, A.; Álvaro, M.; Ferrer, B.; García, H. Metal-Organic Frameworks as Photocatalysts for Solar-Driven Overall Water Splitting. *Chem. Rev.* **2023**, *123*, 445–490. [[CrossRef](#)]
13. Jin, J. Porphyrin-Based Metal-Organic Framework Catalysts for Photoreduction of CO₂: Understanding the Effect of Node Connectivity and Linker Metalation on Activity. *New J. Chem.* **2020**, *44*, 15362–15368. [[CrossRef](#)]

14. Stanley, P.M.; Hemmer, K.; Hegelmann, M.; Schulz, A.; Park, M.; Elsner, M.; Cokoja, M.; Warnan, J. Topology- and Wavelength-Governed CO₂ Reduction Photocatalysis in Molecular Catalyst-Metal–Organic Framework Assemblies. *Chem. Sci.* **2022**, *13*, 12164–12174. [[CrossRef](#)]
15. Majewski, M.B.; Peters, A.W.; Wasielewski, M.R.; Hupp, J.T.; Farha, O.K. Metal–Organic Frameworks as Platform Materials for Solar Fuels Catalysis. *ACS Energy Lett.* **2018**, *3*, 598–611. [[CrossRef](#)]
16. Li, R.; Hu, J.; Deng, M.; Wang, H.; Wang, X.; Hu, Y.; Jiang, H.; Jiang, J.; Zhang, Q.; Xie, Y.; et al. Integration of an Inorganic Semiconductor with a Metal–Organic Framework: A Platform for Enhanced Gaseous Photocatalytic Reactions. *Adv. Mater.* **2014**, *26*, 4783–4788. [[CrossRef](#)]
17. Wang, M.; Wang, D.; Li, Z. Self-Assembly of CPO-27-Mg/TiO₂ Nanocomposite with Enhanced Performance for Photocatalytic CO₂ Reduction. *Appl. Catal. B* **2016**, *183*, 47–52. [[CrossRef](#)]
18. Wang, L.; Jin, P.; Huang, J.; She, H.; Wang, Q. Integration of Copper(II)-Porphyrin Zirconium Metal–Organic Framework and Titanium Dioxide to Construct Z-Scheme System for Highly Improved Photocatalytic CO₂ Reduction. *ACS Sustain. Chem. Eng.* **2019**, *7*, 15660–15670. [[CrossRef](#)]
19. Lin, C.; Han, C.; Zhang, H.; Gong, L.; Gao, Y.; Wang, H.; Bian, Y.; Li, R.; Jiang, J. Porphyrin-Based Metal–Organic Frameworks for Efficient Photocatalytic H₂ Production under Visible-Light Irradiation. *Inorg. Chem.* **2021**, *60*, 3988–3995. [[CrossRef](#)] [[PubMed](#)]
20. Rajasree, S.S.; Li, X.; Deria, P. Physical Properties of Porphyrin-Based Crystalline Metal–organic Frameworks. *Commun. Chem.* **2021**, *4*, 47. [[CrossRef](#)] [[PubMed](#)]
21. Choi, S.; Jung, W.-J.; Park, K.; Kim, S.-Y.; Baeg, J.-O.; Kim, C.H.; Son, H.-J.; Pac, C.; Kang, S.O. Rapid Exciton Migration and Amplified Funneling Effects of Multi-Porphyrin Arrays in a Re(I)/Porphyrinic MOF Hybrid for Photocatalytic CO₂ Reduction. *ACS Appl. Mater. Interfaces* **2021**, *13*, 2710–2722. [[CrossRef](#)]
22. Son, H.-J.; Jin, S.; Patwardhan, S.; Wezenberg, S.J.; Jeong, N.C.; So, M.; Wilmer, C.E.; Sarjeant, A.A.; Schatz, G.C.; Snurr, R.Q.; et al. Light-Harvesting and Ultrafast Energy Migration in Porphyrin-Based Metal–Organic Frameworks. *J. Am. Chem. Soc.* **2013**, *135*, 862–869. [[CrossRef](#)] [[PubMed](#)]
23. Li, Q.; Wang, K.; Wang, H.; Zhou, M.; Zhou, B.; Li, Y.; Li, Q.; Wang, Q.; Shen, H.-M.; She, Y. Metalloporphyrin-Based Metal–Organic Frameworks for Photocatalytic Carbon Dioxide Reduction: The Influence of Metal Centers. *Processes* **2023**, *11*, 1042. [[CrossRef](#)]
24. He, J.; Zhang, Y.; He, J.; Zeng, X.; Hou, X.; Long, Z. Enhancement of Photoredox Catalytic Properties of Porphyrinic Metal–Organic Frameworks Based on Titanium Incorporation via Post-Synthetic Modification. *Chem. Commun.* **2018**, *54*, 8610–8613. [[CrossRef](#)] [[PubMed](#)]
25. Wei, Z.; Song, S.; Gu, H.; Li, Y.; Sun, Q.; Ding, N.; Tang, H.; Zheng, L.; Liu, S.; Li, Z.; et al. Enhancing the Photocatalytic Activity of Zirconium-Based Metal–Organic Frameworks Through the Formation of Mixed-Valence Centers. *Adv. Sci.* **2023**, *10*, 2303206. [[CrossRef](#)]
26. Xu, C.; Liu, H.; Li, D.; Su, J.-H.; Jiang, H.-L. Direct Evidence of Charge Separation in a Metal–Organic Framework: Efficient and Selective Photocatalytic Oxidative Coupling of Amines via Charge and Energy Transfer. *Chem. Sci.* **2018**, *9*, 3152–3158. [[CrossRef](#)] [[PubMed](#)]
27. Chen, X.; Wei, Z.; Li, Y.; Sun, Q.; Ding, N.; Zheng, L.; Liu, S.; Chen, W.; Li, S.; Pang, S. Modulating the Conduction Band of MOFs by Introducing Tiny TiO₂ Nanoparticles for Enhanced Photocatalytic Performance: Importance of the Loading Position. *Inorg. Chem.* **2023**, *62*, 10572–10581. [[CrossRef](#)] [[PubMed](#)]
28. Fang, Z.-B.; Liu, T.-T.; Liu, J.; Jin, S.; Wu, X.-P.; Gong, X.-Q.; Wang, K.; Yin, Q.; Liu, T.-F.; Cao, R.; et al. Boosting Interfacial Charge-Transfer Kinetics for Efficient Overall CO₂ Photoreduction via Rational Design of Coordination Spheres on Metal–Organic Frameworks. *J. Am. Chem. Soc.* **2020**, *142*, 12515–12523. [[CrossRef](#)] [[PubMed](#)]
29. Zhang, A.; Si, D.; Huang, H.; Xie, L.; Fang, Z.; Liu, T.; Cao, R. Partial Metalation of Porphyrin Moieties in Hydrogen-Bonded Organic Frameworks Provides Enhanced CO₂ Photoreduction Activity. *Angew. Chem. Int. Ed.* **2022**, *61*, e202203955. [[CrossRef](#)]
30. Yu, C.-J.; Krzyaniak, M.D.; Fataftah, M.S.; Wasielewski, M.R.; Freedman, D.E. A Concentrated Array of Copper Porphyrin Candidate Qubits. *Chem. Sci.* **2019**, *10*, 1702–1708. [[CrossRef](#)]
31. Wang, L.; Duan, S.; Jin, P.; She, H.; Huang, J.; Lei, Z.; Zhang, T.; Wang, Q. Anchored Cu(II) Tetra(4-Carboxylphenyl)Porphyrin to P25 (TiO₂) for Efficient Photocatalytic Ability in CO₂ Reduction. *Appl. Catal. B* **2018**, *239*, 599–608. [[CrossRef](#)]
32. Jin, P.; Wang, L.; Ma, X.; Lian, R.; Huang, J.; She, H.; Zhang, M.; Wang, Q. Construction of Hierarchical ZnIn₂S₄@PCN-224 Heterojunction for Boosting Photocatalytic Performance in Hydrogen Production and Degradation of Tetracycline Hydrochloride. *Appl. Catal. B* **2021**, *284*, 119762. [[CrossRef](#)]
33. Hartle, M.D.; Prell, J.S.; Pluth, M.D. Spectroscopic Investigations into the Binding of Hydrogen Sulfide to Synthetic Picket-Fence Porphyrins. *Dalton Trans.* **2016**, *45*, 4843–4853. [[CrossRef](#)] [[PubMed](#)]
34. Wang, L.; Jin, P.; Duan, S.; Huang, J.; She, H.; Wang, Q.; An, T. Accelerated Fenton-like Kinetics by Visible-Light-Driven Catalysis over Ironⁱⁱⁱ Porphyrin Functionalized Zirconium MOF: Effective Promotion on the Degradation of Organic Contaminants. *Environ. Sci. Nano* **2019**, *6*, 2652–2661. [[CrossRef](#)]
35. Ma, C.; Wolterbeek, H.T.; Denkova, A.G.; Serra Crespo, P. Porphyrinic Metal–Organic Frameworks as Molybdenum Adsorbents for the ⁹⁹Mo/^{99m}Tc Generator. *Inorg. Chem. Front.* **2023**, *10*, 2239–2249. [[CrossRef](#)]

36. Wang, N.; Liu, S.; Sun, Z.; Han, Y.; Xu, J.; Xu, Y.; Wu, J.; Meng, H.; Zhang, B.; Zhang, X. Synergistic Adsorption and Photocatalytic Degradation of Persistent Synthetic Dyes by Capsule-like Porphyrin-Based MOFs. *Nanotechnology* **2021**, *32*, 465705. [[CrossRef](#)] [[PubMed](#)]
37. Yao, B.; Peng, C.; He, Y.; Zhang, W.; Zhang, Q.; Zhang, T. Conjugated Microspheres FeTCPP-TDI-TiO₂ with Enhanced Photocatalytic Performance for Antibiotics Degradation Under Visible Light Irradiation. *Catal. Lett.* **2016**, *146*, 2543–2554. [[CrossRef](#)]
38. Liu, X.; Qi, W.; Wang, Y.; Lin, D.; Yang, X.; Su, R.; He, Z. Rational Design of Mimic Multienzyme Systems in Hierarchically Porous Biomimetic Metal–Organic Frameworks. *ACS Appl. Mater. Interfaces* **2018**, *10*, 33407–33415. [[CrossRef](#)] [[PubMed](#)]
39. Smith, M.R.; Martin, C.B.; Arumuganainar, S.; Gilman, A.; Koel, B.E.; Sarazen, M.L. Mechanistic Elucidations of Highly Dispersed Metalloporphyrin Metal–Organic Framework Catalysts for CO₂ Electroreduction. *Angew. Chem. Int. Ed.* **2023**, *62*, e202218208. [[CrossRef](#)]
40. Yu, K.; Lee, Y.-R.; Seo, J.Y.; Baek, K.-Y.; Chung, Y.-M.; Ahn, W.-S. Sonochemical Synthesis of Zr-Based Porphyrinic MOF-525 and MOF-545: Enhancement in Catalytic and Adsorption Properties. *Microporous Mesoporous Mater.* **2021**, *316*, 110985. [[CrossRef](#)]
41. Zhao, Y.; Kuang, Y.; Liu, M.; Wang, J.; Pei, R. Synthesis of Metal–Organic Framework Nanosheets with High Relaxation Rate and Singlet Oxygen Yield. *Chem. Mater.* **2018**, *30*, 7511–7520. [[CrossRef](#)]
42. Cao, X.; Tong, R.; Tang, S.; Jang, B.W.-L.; Mirjalili, A.; Li, J.; Guo, X.; Zhang, J.; Hu, J.; Meng, X. Design of Pd–Zn Bimetal MOF Nanosheets and MOF-Derived Pd_{3.9}Zn_{6.1}/CNS Catalyst for Selective Hydrogenation of Acetylene under Simulated Front-End Conditions. *Molecules* **2022**, *27*, 5736. [[CrossRef](#)] [[PubMed](#)]
43. Zhai, G.; Liu, Y.; Lei, L.; Wang, J.; Wang, Z.; Zheng, Z.; Wang, P.; Cheng, H.; Dai, Y.; Huang, B. Light-Promoted CO₂ Conversion from Epoxides to Cyclic Carbonates at Ambient Conditions over a Bi-Based Metal–Organic Framework. *ACS Catal.* **2021**, *11*, 1988–1994. [[CrossRef](#)]
44. Madhusudan Reddy, K.; Gopal Reddy, C.V.; Manorama, S.V. Preparation, Characterization, and Spectral Studies on Nanocrystalline Anatase TiO₂. *J. Solid. State Chem.* **2001**, *158*, 180–186. [[CrossRef](#)]
45. Sheng, W.; Wang, X.; Wang, Y.; Chen, S.; Lang, X. Integrating TEMPO into a Metal–Organic Framework for Cooperative Photocatalysis: Selective Aerobic Oxidation of Sulfides. *ACS Catal.* **2022**, *12*, 11078–11088. [[CrossRef](#)]
46. da Trindade, L.G.; Borba, K.M.N.; Trench, A.B.; Zanchet, L.; Teodoro, V.; Pontes, F.M.L.; Longo, E.; Mazzo, T.M. Effective Strategy to Coupling Zr-MOF/ZnO: Synthesis, Morphology and Photoelectrochemical Properties Evaluation. *J. Solid. State Chem.* **2021**, *293*, 121794. [[CrossRef](#)]
47. Mette, G.; Sutter, D.; Gurdal, Y.; Schnidrig, S.; Probst, B.; Iannuzzi, M.; Hutter, J.; Alberto, R.; Osterwalder, J. From Porphyrins to Porphyrins: Adsorption Study and Metalation of a Molecular Catalyst on Au(111). *Nanoscale* **2016**, *8*, 7958–7968. [[CrossRef](#)] [[PubMed](#)]
48. Gottfried, J.M.; Flechtner, K.; Kretschmann, A.; Lukasczyk, T.; Steinrück, H.-P. Direct Synthesis of a Metalloporphyrin Complex on a Surface. *J. Am. Chem. Soc.* **2006**, *128*, 5644–5645. [[CrossRef](#)]
49. Diller, K.; Papageorgiou, A.C.; Klappenberger, F.; Allegretti, F.; Barth, J.V.; Auwärter, W. In Vacuo Interfacial Tetrapyrrole Metallation. *Chem. Soc. Rev.* **2016**, *45*, 1629–1656. [[CrossRef](#)]
50. Crake, A.; Christoforidis, K.C.; Gregg, A.; Moss, B.; Kafizas, A.; Petit, C. The Effect of Materials Architecture in TiO₂/MOF Composites on CO₂ Photoreduction and Charge Transfer. *Small* **2019**, *15*, 1805473. [[CrossRef](#)] [[PubMed](#)]
51. Lu, Z.; Gao, J.; Rao, S.; Jin, C.; Jiang, H.; Shen, J.; Yu, X.; Wang, W.; Wang, L.; Yang, J.; et al. A Multifunctional Membrane Based on TiO₂/PCN-224 Heterojunction with Synergistic Photocatalytic-Photothermal Activity under Visible-Light Irradiation. *Appl. Catal. B* **2024**, *342*, 123374. [[CrossRef](#)]
52. Wang, Y.; Wang, X.; Lu, H.; Gu, Z.; Chen, L. Au-Nanorod-Modified PCN-222(Cu) for H₂ Evolution from HCOOH Dehydrogenation by Photothermally Enhanced Photocatalysis. *Chem. Commun.* **2022**, *58*, 8520–8523. [[CrossRef](#)] [[PubMed](#)]

Disclaimer/Publisher’s Note: The statements, opinions and data contained in all publications are solely those of the individual author(s) and contributor(s) and not of MDPI and/or the editor(s). MDPI and/or the editor(s) disclaim responsibility for any injury to people or property resulting from any ideas, methods, instructions or products referred to in the content.